2023 IEEE/RSJ International Conference on Intelligent Robots and Systems (IROS)
October 1-5, 2023. Detroit, USA

HALO: A Safe, Coaxial, and Dual-Ducted UAV without Servo

Haotian Li*, Nan Chen*, Fanze Kong, Yuying Zou, Shenji Zhou,
Dongjiao He and Fu Zhang

***Abstract*— This paper presents a novel uncrewed aerial vehicle (UAV) design named HALO, which stands for "harmless aerial limber robot". HALO uses a swashplateless mechanism to generate a moment for pitch and roll control without requiring additional actuators such as servo, reducing the number of components needed for control and enhancing reliability. Its reduced weight and number of actuators improve payload capacity and maneuverability. Meanwhile, HALO's coaxial duct design improves safety and aerodynamic efficiency. Experimental tests, including figure-of-eight trajectory tracking, wind gust and stick poking disturbances, hover efficiency comparison, and actual flight with collision is conducted to confirm HALO's robustness and exceptional safety characteristics, suggesting it as a promising design for various applications.**

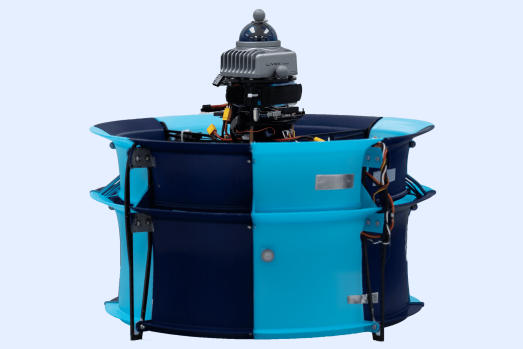

Fig. 1. Our coaxial and dual-ducted UAV, named HALO.

I. INTRODUCTION

Uncrewed aerial vehicles (UAVs) have undergone significant advancements in their design, encompassing a wide range of types and sizes. These advancements have drawn considerable attention in the domains of mechanical design and control algorithm development [1]. Among the various UAV types, the ducted coaxial-rotor configuration has emerged as a promising design due to its distinctive structure that permits its adaptation to complex environments and flight missions. In general, the coaxial ducted UAV design provides superior stability, control, safety, propulsion efficiency, and payload capacity compared to traditional UAVs [2]–[7]. Furthermore, the coaxial design requires fewer motors and propellers, leading to a lightweight body, cost-effectiveness, and higher stability. Although the total thrust generated by coaxial propulsion may be lower than that of two separated propellers [8], [9], the motors with vertically overlapped installation enables better maneuverability due to its more compact structure. The use of two rotors in a coaxial configuration also reduces the risk of crashes as the UAV can still maintain altitude even if one of the rotors malfunctions.

The design of coaxial UAVs significantly impacts their flight performance and control logic. Conventionally, these UAVs are powered by a pair of coaxially arranged motors. The incorporation of a duct in such systems is a favourable option owing to the enhancement in efficiency and safety it offers. Two types of actuation principles are utilized in coaxial UAVs: one involves the installation of motors on the UAV frame, along with a vane positioned below the blade that can be operated by a servo to deflect airflow and generate vector force for aircraft control [10]–[12]. While this control device is simple to install and operate, the vane adds weight to the UAV and is not conducive to efficiency improvement. Moreover, operating the servo to generate the aerodynamic moment requires additional time, thereby reducing the flexibility of the UAV and increasing its vertical size. The other one involves a motor with a swashplate that can be operated by servos to control the aircraft by cyclic pitch angle control of the blade, thereby allowing the lift generated by the motor to become a controllable vector lift [13]–[15]. Whereas, this design has a complex structure since the motor typically needs a special design to install with the swashplate or even the swashplate itself has many mechanical components. The increased weight and complexity deteriorate the agility, efficiency, and reliability of the UAV. Overall, while the coaxial dual-rotor configuration holds promise for UAVs, the complexities of the actuation system limit its performance.

To address the aforementioned design issues, Paulos and Yim introduced the swashplateless mechanism [16] to UAVs. The swashplateless mechanism is a passive structure that can generate lateral moment by controlling the high-frequency acceleration and deceleration of the motor without the need for additional actuators. The principle of the swashplateless mechanism has been utilized in the design of a coaxial configuration UAV detailed in [17]. However, the swashplateless coaxial UAV in [17] employs open blades and lacks a protective duct for the UAV structure. The UAV also bring difficulties for landing gear design posing challenges to the aircraft's maneuverability and structure stiffness, and require specialized motor driving device restricting the potential for broader research applications. Moreover, since the design in [17] has only one motor with the swashplateless mechanism and another motor equips usual propeller, the redundancy of actuators and maximum moment output are restricted. These deficiencies not only pose inherent risks to UAV safety but

*These two authors contribute equally to this work.
All authors are with the Department of Mechanical Engineering, The University of Hong Kong (HKU), Pokfulam, Hong Kong. {*haotianl,cnchen,kongfz,zyycici,shenjizhou,hdj65822*}*@connect.hku.hk*, {*fuzhang*} *@hku.hk*.

2023 IEEE/RSJ International Conference on Intelligent Robots and Systems (IROS) | 978-1-6654-9190-7/23/$31.00 ©2023 IEEE | DOI: 10.1109/IROS55552.2023.10341923

Authorized licensed use limited to: The University of Hong Kong Libraries. Downloaded on March 28,2024 at 05:31:34 UTC from IEEE Xplore. Restrictions apply.

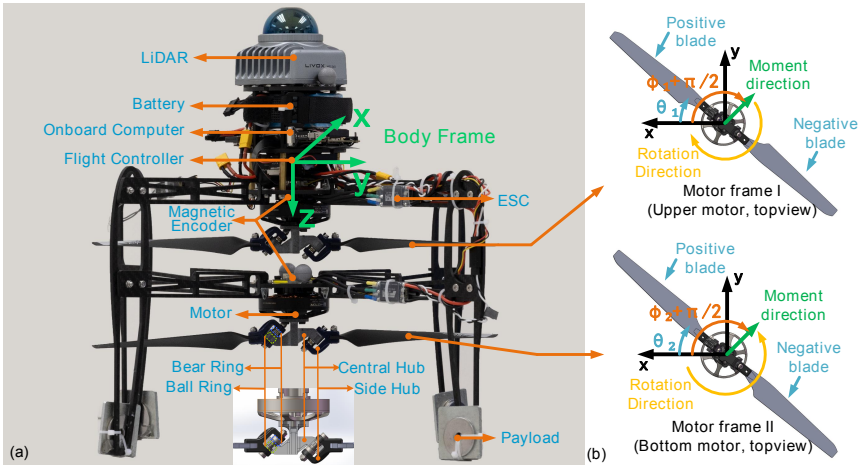

Fig. 2. Structure illustration. (a) The structure of HALO and the swashplateless actuator. (b) The definition of motor frames and angles.

TABLE I
SPECIFICATIONS OF HALO

Item	Parameter
Diameter	39.1 cm
Height	33.8 cm
Total weight (with battery)	1.34 kg
Thrust weight ratio	3.2
Hover current	8.8 A
Battery	6S, 750 mAh

also impede its versatility.

In this paper, a novel design of coaxial UAV, named HALO, is developed to incorporate a swashplateless mechanism and coaxial duct to address the aforementioned issues. The coaxial duct design significantly enhances aerodynamic efficiency, safeguards the blades, and integrates the landing gear with the fuselage to improve the aircraft's maneuverability. Two swashplateless mechanisms are installed on the two motors separately, thereby enhancing the control effect of the aircraft while providing a certain redundancy of actuators. This design offers enhanced safety, improved propulsion efficiency, and greater payload capacity compared to existing coaxial designs, thus making it a viable option for operation in complex and narrow environments. Various experiments have been conducted to validate the performance of the proposed design, which are shown in following sections.

II. SYSTEM DESIGN

A. UAV Structure and Avionics

We designed and manufactured a coaxial ducted UAV called HALO, which could be used for safe exploration and simultaneous localization and mapping (SLAM) in confined spaces [18]–[21]. It is equipped with a Livox Mid-360 LiDAR and an onboard computer Khadas VIM3. The LiDAR's non-repeating scan mode, combined with its 360° × 59° field of view, makes it ideal for generating dense point clouds in indoor environments. To ensure compactness and enhance safety during indoor flights, we employed the coaxial duct design. The mechanical design of HALO is straightforward and easy to assemble, given that it is a prototype, hence we utilized carbon fiber plates and 3D printed PLA materials for its construction. The composition of the aircraft and the duct can be seen from figures. 1 and 2.

The avionics system of the UAV is centered on the Pixhawk 4 mini flight controller, which is securely mounted to the fuselage. Two brushless motors and two magnetic encoders are linked to the controller, governing all aircraft movements and precisely measuring the rotor angle. A swashplateless mechanism is employed to generate lift and moment through rotational motion of the motors. The resultant UAV design boasts a diameter of 39.1 cm and a weight of 1.34 kg, and further detailed parameters are shown in Table I.

B. Duct design

The UAV featuring a ducted structure exhibits superior safety characteristic in comparison to those equipped with an open-rotor structure. This is attributed to the presence of an external duct that precludes direct rotor-environment contact, as well as the enhancement of thrust production through the augmentation of air flow at the duct's lip, when compared to open-rotor configurations with equivalent rotor blade size [22]–[24]. Most ducted coaxial UAVs are equipped with only one duct, but for HALO, two coaxial ducts are installed on the UAV chassis, as shown in Fig. 1. When equipped with two coaxial ducts, the efficiency and thrust of the UAV will be improved compared to the single duct state [25]. The use of dual ducts equips our UAV with new features that have not been found in previous coaxial UAVs.

C. Swashplateless Actuator

The swashplateless actuator comprises several key components, including a T-MOTOR MN5006 brushless DC motor, an improved swashplateless mechanism mounted on the motor's rotor, a pair of propeller blades, and a magnetic encoder (model AS5600) installed on the motor shaft. The actuator is capable of generating both thrust and moment, with thrust being generated directly by the propeller and moment being produced by the unbalanced thrust of the blades induced by cyclic blade pitch control [26], [27]. This technique is commonly employed in helicopters through

Authorized licensed use limited to: The University of Hong Kong Libraries. Downloaded on March 28,2024 at 05:31:34 UTC from IEEE Xplore. Restrictions apply.

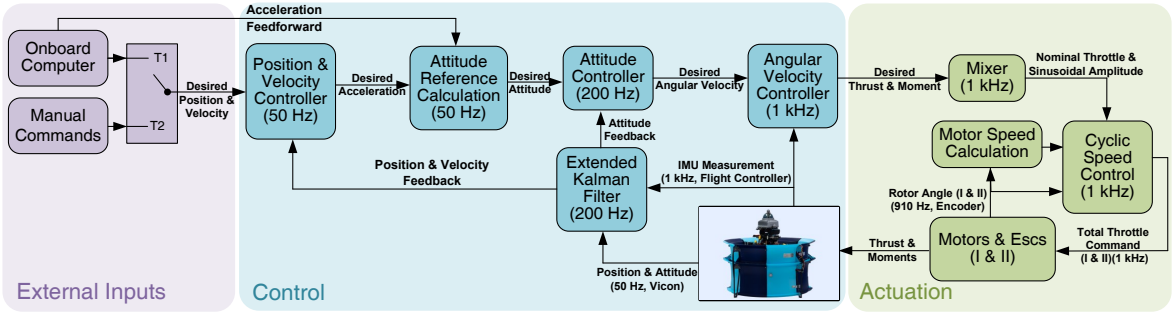

Fig. 3. Control system overview.

servos and swashplates. However, the swashplateless actuator in HALO is entirely passive, and hence no additional servos and complicated swashplate are required.

The swashplateless mechanism with improved structure is illustrated in Fig. 2. The side hubs are connected to the central hub via two passive hinges in an asymmetrical manner. The rotation of these hinges, as a result of blade inertia, is induced by the periodic acceleration and deceleration of the motor, also known as motor speed modulation. This leads to variations in pitch angle changes of the positive and negative blades, with the blade exhibiting an increased pitch angle producing greater thrust while the blade displaying a decreased pitch angle generates less thrust, ultimately resulting in the generation of a net moment. The original design and the functioning principles of the mechanism are further elaborated upon in [8], [16]. Different from the original design, the improved design used in this UAV features the addition of ball bearings and pressure bearings, aimed at mitigating the friction generated by the high-frequency rotation of the hinges and providing a smoother output of moment with more rapid response when compared to the original design. The propulsion system is shown in Fig. 2.

III. Control and Actuation

A. Control System Overview

Fig. 3 provides an overview of the control system for HALO, which is based on the software framework of PX4. The position controller has two modes: the manual mode and autonomous mode. In the manual mode, the input of the remote controller is directly mapped to the velocity reference. In the autonomous mode, the position reference is used as the input of the position controller, and the references of velocity and acceleration are used as feed-forward terms.

The control part is the standard realization of PX4 while the actuation part are specifically designed for actuating the swashplateless mechanism, and hence should be highlighted. The operating frequencies of the mixer and the cyclic speed control are dependent on the output frequency of the angular velocity controller (i.e., the measurement frequency of the inertial measurement unit (IMU)). Therefore, we set the measurement frequency of the IMU to 1 kHz, allowing the cyclic speed control to run at the same frequency for processing each measurement from the two magnetic encoders with a measurement frequency of 910 Hz. In addition to the rotor angle, we incorporated a motor speed calculation to calculate the motor speed based on the measured rotor angle, enabling dynamic lag angle compensation for the swashplateless mechanism. The motor speed calculation relies on the differential of the motor angle, and a Butterworth low-pass filter is applied to suppress the noise caused by the differential. The total throttles generated by cyclic speed control are transmitted to a standard Electronic Speed Controllers (ESCs) (model T-MOTOR F35A 3-6S) using the DShot600 communication protocol. This protocol is suitable for high-frequency speed modulation of the motor since it has a very short communication delay of 26.7 us.

B. Dynamic Model and Actuation Principle

As shown in Fig. 2 (a), a body frame $\mathcal{B}$ is attached to UAV's center of mass whose x-axis points to the UAV's head and z-axis is opposite to the UAV's thrust direction. Defining a static inertial frame $\mathcal{I}$, the dynamics of translation and rotation of HALO can be represented in a standard rigid motion as

$$\begin{bmatrix} m\boldsymbol{I} & \mathbf{0} \\ \mathbf{0} & \boldsymbol{J}^{\mathcal{B}} \end{bmatrix} \begin{bmatrix} \dot{\boldsymbol{v}}^{\mathcal{I}} \\ \dot{\boldsymbol{\omega}}^{\mathcal{B}} \end{bmatrix} + \begin{bmatrix} \mathbf{0} \\ \widehat{\boldsymbol{\omega}}^{\mathcal{B}} \boldsymbol{J}^{\mathcal{B}} \boldsymbol{\omega}^{\mathcal{B}} \end{bmatrix} = \begin{bmatrix} \boldsymbol{f}_G^{\mathcal{I}} \\ \mathbf{0} \end{bmatrix} + \begin{bmatrix} \boldsymbol{R}^{\mathcal{IB}} \boldsymbol{f}_T^{\mathcal{B}} \\ \boldsymbol{\tau}^{\mathcal{B}} \end{bmatrix} \quad (1)$$

where m, $\boldsymbol{I}$, and $\boldsymbol{J}^{\mathcal{B}}$ stand for the mass, the identity matrix in $\mathbb{R}^{3\times3}$ and the inertia matrix in the body frame, respectively. $\boldsymbol{\omega}^{\mathcal{B}}$ is the angular velocity vector represented in the body frame while $\widehat{\boldsymbol{\omega}}^{\mathcal{B}}$ is the skew-symmetric cross-product matrix of $\boldsymbol{\omega}^{\mathcal{B}}$, $\boldsymbol{v}^{\mathcal{I}}$ is the velocity vector represented in the inertial frame. $\boldsymbol{f}_G^{\mathcal{I}} = \begin{bmatrix} 0 & 0 & mg \end{bmatrix}^T$ stands for the gravity in the inertial frame and the thrust vector in body frame is $\boldsymbol{f}_T^{\mathcal{B}} = \begin{bmatrix} 0 & 0 & f_T^{\mathcal{B}} \end{bmatrix}^T$. $\boldsymbol{\tau}^{\mathcal{B}} = \begin{bmatrix} \tau_x^{\mathcal{B}} & \tau_y^{\mathcal{B}} & \tau_z^{\mathcal{B}} \end{bmatrix}^T$ is the moment vector. $\boldsymbol{R}^{\mathcal{IB}}$ is the rotation matrix representing the coordinate transformation from the body frame $\mathcal{B}$ to the inertial frame $\mathcal{I}$.

The thrust $f_T^{\mathcal{B}}$ is generated by the two propellers driven by the motors, while the z-axis component of the moment vector $\tau_z^{\mathcal{B}}$ comes from the differential anti-torque of the two motors rotating in opposite directions. The 2D moment vector that lies on the x-y plane of the body frame (i.e., $\begin{bmatrix} \tau_x^{\mathcal{B}} & \tau_y^{\mathcal{B}} \end{bmatrix}^T$) is the collective moments produced by the two swashplateless mechanisms, since the moment magnitude and direction within the propeller plane (i.e., the x-y plane of the body frame) are both controllable by the swashplateless mechanisms.

Authorized licensed use limited to: The University of Hong Kong Libraries. Downloaded on March 28,2024 at 05:31:34 UTC from IEEE Xplore. Restrictions apply.

C. Mixer Design

To describe the direction of the moment generated by the swashplateless mechanism and the angles used for the cyclic speed control of motor, two motor frames are defined. Despite the two motors rotating in opposite directions, the two motor frames have the same form. The y-axes of the motor frames are aligned with the x-axis of the body frame, as illustrated in Fig. 2 (b). The absolute angle of the rotor, θ_i, is defined as the angle between the x-axis and the positive blade, irrespective of the rotation direction. In the motor coordinate frame, the moment direction is represented as $\phi_i + \pi/2$, as depicted in Fig. 2 (b). Due to the inherent 90° rotation between the body frame and the motor frame, we can directly use ϕ_i to represent the moment direction in the body frame without any coordinate transformation.

The mixer is designed to calculate all actuator inputs that can produce the desired thrust $f_{T,d}^{\mathcal{B}}$ and moment $\boldsymbol{\tau}_d^{\mathcal{B}}$ represented in the body frame. Based on the actuation principle of the UAV, the mapping from the output of the actuators to the body thrust and moment is given by:

$$\begin{bmatrix} f_T^{\mathcal{B}} \\ \tau_x^{\mathcal{B}} \\ \tau_y^{\mathcal{B}} \\ \tau_z^{\mathcal{B}} \end{bmatrix} = \begin{bmatrix} 1 & 1 & 0 & 0 \\ 0 & 0 & \cos(\phi_1) & \cos(\phi_2) \\ 0 & 0 & \sin(\phi_1) & \sin(\phi_2) \\ -\kappa & \kappa & 0 & 0 \end{bmatrix} \begin{bmatrix} T_1 \\ T_2 \\ \tau_1 \\ \tau_2 \end{bmatrix}, \quad (2)$$

where T_i, τ_i, and ϕ_i $(i = 1, 2)$ are the thrusts of propeller, the moments generated by the swashplateless mechanism of motor, and the moments' direction in the body frame, respectively. κ is a constant coefficient for mapping the motor thrust to the motor anti-torque. It is should be noted that in (3), there are six independent actuation variables, $T_1, T_2, \tau_1, \tau_2, \phi_1$, and ϕ_2 while the control actions they produce are only four, $f_T^{\mathcal{B}}$, $\tau_x^{\mathcal{B}}$, $\tau_y^{\mathcal{B}}$, and $\tau_z^{\mathcal{B}}$. This leads to that there are multiple ways to generate the control actions through changing the independent actuation variables. To eliminate the redundancy in actuation, we fix $\phi_1 = \phi_2 = \phi$ and define $\tau_t = \tau_1 + \tau_2$, which means the moments generated from two swashplateless mechanisms have the same direction and amplitude. Then,

$$\begin{bmatrix} f_T^{\mathcal{B}} \\ \tau_x^{\mathcal{B}} \\ \tau_y^{\mathcal{B}} \\ \tau_z^{\mathcal{B}} \end{bmatrix} = \begin{bmatrix} 1 & 1 & 0 & 0 \\ 0 & 0 & 1 & 0 \\ 0 & 0 & 0 & 1 \\ -\kappa & \kappa & 0 & 0 \end{bmatrix} \begin{bmatrix} T_1 \\ T_2 \\ \tau_t \cos(\phi) \\ \tau_t \sin(\phi) \end{bmatrix}. \quad (3)$$

In the state near to hover, the actuation efforts are approximately proportional to the actuator commands as follows:

$$\begin{bmatrix} T_1 \\ T_2 \\ \tau_t \cos(\phi) \\ \tau_t \sin(\phi) \end{bmatrix} = \begin{bmatrix} K_t & 0 & 0 & 0 \\ 0 & K_t & 0 & 0 \\ 0 & 0 & K_a & 0 \\ 0 & 0 & 0 & K_a \end{bmatrix} \begin{bmatrix} C_1 \\ C_2 \\ A_x \\ A_y \end{bmatrix}, \quad (4)$$

where C_1 and C_2 are the nominal throttle, A_x and A_y are the amplitudes of sinusoidal throttle that drives the swashplateness to produce the lateral moment in x- and y-directions (the moment in the propeller plane, see the following section). K_t and K_a are proportion coefficients representing the proportional mapping from the nominal throttle to the thrust, and from the amplitude of sinusoidal throttle to the moment of swashplateless mechanism, respectively.

Given the desired thrust $f_{T,d}^{\mathcal{B}}$ and the desired moment vector $\boldsymbol{\tau}_d^{\mathcal{B}} = \begin{bmatrix} \tau_{x,d}^{\mathcal{B}} & \tau_{y,d}^{\mathcal{B}} & \tau_{z,d}^{\mathcal{B}} \end{bmatrix}^T$, combining (3) and (4), we can invert the coefficient matrix and finally determine the desired throttles as

$$\begin{bmatrix} C_{1,d} \\ C_{2,d} \\ A_{x,d} \\ A_{y,d} \end{bmatrix} = \begin{bmatrix} \frac{1}{2K_t} & 0 & 0 & \frac{-1}{2\kappa K_t} \\ \frac{1}{2K_t} & 0 & 0 & \frac{1}{2\kappa K_t} \\ 0 & \frac{1}{K_a} & 0 & 0 \\ 0 & 0 & \frac{1}{K_a} & 0 \end{bmatrix} \begin{bmatrix} f_{T,d}^{\mathcal{B}} \\ \tau_{x,d}^{\mathcal{B}} \\ \tau_{y,d}^{\mathcal{B}} \\ \tau_{z,d}^{\mathcal{B}} \end{bmatrix}, \quad (5)$$

where the $C_{1,d}$ and $C_{2,d}$ are the desired nominal throttle, and $A_{x,d}$ and $A_{y,d}$ are the desired amplitude of sinusoidal throttle in x- and y-directions, respectively.

D. Cyclic Speed Control of Motor

Cyclic speed control is applied on motor to generate the lateral moment through swashplateless mechanism. To prevent undesired vibration caused by motor speed modulation, a sinusoidal signal is employed for two motors. The motor throttle command U_i $(i = 1, 2)$ is designed as

$$\begin{bmatrix} U_1 \\ U_2 \end{bmatrix} = \begin{bmatrix} C_1 \\ C_2 \end{bmatrix} + \begin{bmatrix} A_1 & 0 \\ 0 & A_2 \end{bmatrix} \begin{bmatrix} \cos(\theta_1 - \phi_1 + \gamma_0) \\ \cos(\theta_2 - \phi_2 + \gamma_0) \end{bmatrix}, \quad (6)$$

where C_i, A_i, ϕ_i, and θ_i $(i = 1, 2)$ are the nominal throttles, sinusoidal amplitudes, moments' direction, and the motors' rotor angles measured by the magnetic encoders, respectively. The γ_0 is a lead angle added to compensate the lag angle of moment direction caused by blades' inertia and can be calibrated in advance. According to experiment data measured by a 6-axis force sensor in a test stand, the γ_0 can be approximately fitted as a quadratic function of the rotor speed, which is

$$\gamma_0 = (a\,|\omega|^2 + b\,|\omega| + c) * \mathrm{sign}(\omega), \quad (7)$$

where ω is the calculated motor speed, and a, b, and c are the coefficients of the quadratic function. The sign of γ_0 is decided by the sign of rotor speed since the direction of lag angle is coincident with the rotation direction.

Since the thrust and moment need to be equally distributed to two motors, leads to

$$\begin{aligned} C_1 &= C_{1,d} \\ C_2 &= C_{2,d} \\ A_1 &= A_2 = \frac{1}{2}\sqrt{A_{x,d}^2 + A_{y,d}^2} \\ \phi_1 &= \phi_2 = \phi = \mathrm{atan2}(A_{y,d},\ A_{x,d}). \end{aligned} \quad (8)$$

Once the $C_{1,d}$, $C_{1,d}$, $A_{x,d}$, and $A_{y,d}$ in (5) are obtained, they are mapped by (8) and then substituted into (6) to generate the total throttles $U_{i,d}$ which are finally sent to the ESCs for execution.

Authorized licensed use limited to: The University of Hong Kong Libraries. Downloaded on March 28,2024 at 05:31:34 UTC from IEEE Xplore. Restrictions apply.

IV. Experiments

This section is to comprehensively evaluate the performance, robustness, and safety of HALO through a series of experimental tests. Firstly, we assess the control performance of the UAV by conducting a 3D figure-of-eight trajectory tracking experiment. Secondly, we investigate the performance of disturbance rejection, including hover under wind gust and stick poking. Thirdly, we compare the power efficiency of HALO with its two variants. Finally, we carry out a flight experiment in an environment containing several obstacles to evaluate the UAV's safety characteristics. The experimental procedures are available in the accompanying videos.

A. Tracking of a 3D Figure-of-eight Trajectory

To evaluate the tracking performance of HALO, we designed a 3D figure-of-eight trajectory, as illustrated in Fig. 4. The trajectory includes displacement in three directions (i.e., 3.6 m, 1.2 m, and 1.0 m in the x-, y-, and z-axes, respectively), and was executed five times with a period of 6 s. In the first and last cycles, the trajectory period was increased to 1.5 times the normal period (i.e., 9 s) to ensure smooth processes of acceleration and deceleration. The trajectory reference, including references for position, velocity, and acceleration, was generated by a ROS node running on the onboard computer and sent to the flight controller through MAVROS and USB port. The position feedback was provided by a motion capture system (i.e., Vicon). The tracking results are depicted in Fig. 5. The position feedback successfully tracked the reference position in all three directions, albeit with a small phase delay. The maximum absolute position errors are 0.468 m, 0.335 m, and 0.067 m in the x-, y-, and z-axes, respectively, while the velocity errors are 0.772 m/s, 0.454 m/s, and 0.163 m/s in the same sequence. Although the frequency of the y-axis reference position is twice that of the x-axis, the amplitude of the x-axis is still larger, resulting in a higher velocity reference in the x-axis than in the y-axis (about 1.8 m/s versus 1.3 m/s). The higher velocity reference make the tracking more challenging, leading to the maximum absolute errors of position and velocity appearing in the x-axis. The experimental results confirm that the swashplateless mechanism can provide sufficient lateral moment to enable the UAV to track the 3D trajectory and can be used to replace traditional actuation methods in coaxial UAVs (e.g., servo and vane).

B. Disturbance Rejection

To evaluate the disturbance rejection performance of HALO, we conducted two experiments: (i) hover with wind gust disturbance and (ii) hover with stick poking disturbance. The position feedback was provided by a motion capture system (Vicon).

1) Hover under wind gust: Fig. 6 (a) depicts a configuration in which a fan is located 1-m away from HALO's hovering position, thereby generating a wind gust. Initially, the fan is turned off, and HALO attains a stable pose before

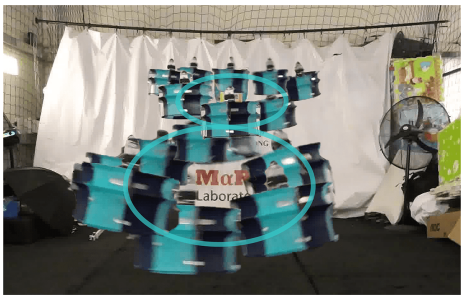

Fig. 4. Overlaid snapshots of HALO when it is tracking the 3D figure-of-eight trajectory.

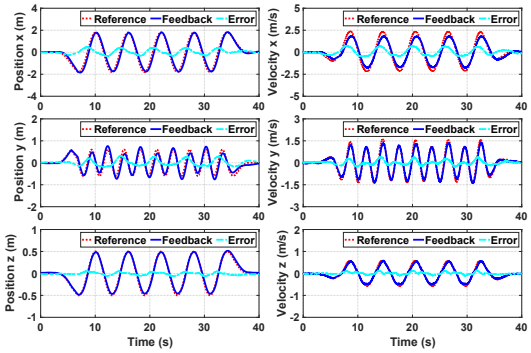

Fig. 5. Position, velocity and their errors during tracking a 3D figure-of-eight trajectory.

the fan is activated to produce a wind with a speed of approximately 5 m/s. After the wind disturbance, the fan is switched off to eliminate the gust. The position error of the UAV is primarily affected along the y-axis since the wind gust is exerted in this direction, as illustrated in Fig. 7. The figure shows that the position error increases immediately after the fan is turned on, reaching a maximum value of 12.3 cm. The position error then decreases and converges to zero due to the integrator of the position controller. In this instance, the UAV tilted its roll angle by approximately 3.6° to produce a thrust component that could counteract the force induced by the wind. When the fan is turned off, the output of the integrator causes the UAV to move closer to the fan, resulting in a maximum position error of 11.8 cm. Finally, the position error decays as the integrator output is reduced to a value close to the hover state.

2) Stick poking: In contrast to the wind gust disturbance experiment that involved no physical contact, the poking disturbance experiment entailed using a rigid stick to apply a force to the UAV body in the y-axis direction, as depicted in Fig. 6 (b). We applied the poking disturbance three times with similar forces to evaluate the UAV's robustness and demonstrate its safety characteristics under active impact from external disturbances. The results, as shown in Fig. 8, reveal three position ripples in the y-axis direction, with a maximum absolute position error of 11.4 cm. In response to the external force, the attitude roll rapidly adjusted to generate a lateral thrust component, thereby maintaining the UAV's hover position and resulting in a maximum absolute attitude roll error of 4.9°. Despite the consecutive poking, the UAV remained in its original position, indicating its robustness to external forces resulting from hard contact, as well as its ability to avoid structural damage due to external

Authorized licensed use limited to: The University of Hong Kong Libraries. Downloaded on March 28,2024 at 05:31:34 UTC from IEEE Xplore. Restrictions apply.

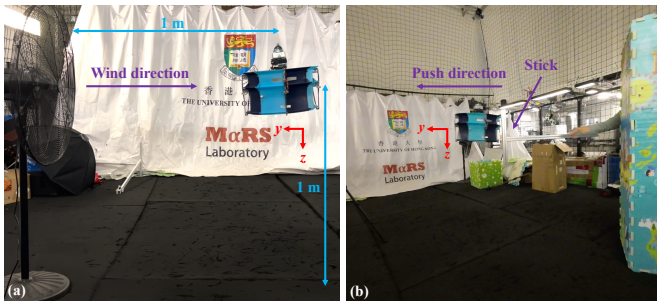

Fig. 6. The setup of the disturbance experiments. (a) The setup for wind gust experiment. (b) The setup for stick poking experiment.

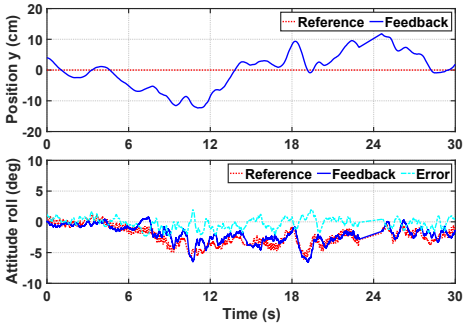

Fig. 7. Position, attitude, and their errors when hovering in the wind gust.

poking, thereby reinforcing its safety characteristics.

C. Comparison of Flight Efficiency

Since the previous UAVs with roughly similar weight as HALO lacked ducts and didn't optimize or calculate power consumption, we evaluated HALO's three different types to illustrate how its duct structures can improve flight efficiency: HALO (standard design with duct, 1344 g), variant I without duct but with payload (1344 g), and variant II without duct nor payload (1117 g). Our findings suggest that when the UAVs have the same weight, the standard design with duct yields a 5.23% reduction in mean power consumption (i.e., 199.5 W versus 210.6 W) when compared to the non-duct variant (i.e., variant I). The variant II has a lighter weight, leading to lower power consumption (i.e., 169.9 W); however, it lacks the safety feature provided by the duct structure and may incur damage to the propeller blade or swashplateless mechanism if it collides with obstacles. In terms of efficiency (defined as the ratio of weight to power consumption), the results are shown in Fig. 9, where the median and mean values are represented by the blue line and green "+", respectively. The three variants achieved power efficiencies of 6.74 g/W, 6.38 g/W, and 6.57 g/W, respectively, with HALO achieving the highest efficiency. According to the momentum theory [28], [29], a UAV's efficiency tends to decrease with increased weight under the same conditions, which favors variant II more. Nevertheless, our results suggest that HALO with 1344-g due to the duct structure still has a higher efficiency than the variant II with 1117-g, confirming the efficiency of the use of ducts.

D. Flight in an Environment with Obstacles

To validate the safety features of HALO, we designed an experimental setup comprising multiple obstacles, including

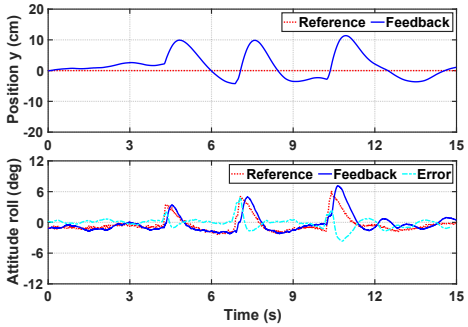

Fig. 8. Position, attitude, and their errors in the disturbance experiment of stick poking.

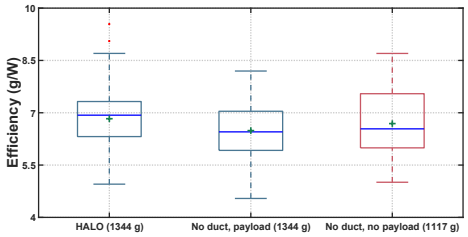

Fig. 9. Hover efficiency of different configurations. The voltage and current fluctuations during the hovering process caused some outliers in the hovering efficiency of HALO.

two fans and a pillar, as illustrated in Fig. 10. To simulate actual flight conditions, we manually maneuvered the UAV through the obstacles, intentionally inducing collisions in the process. The virtual flight trajectory is depicted by the yellow line in Fig. 10, while the actual flight trajectory, as measured by Vicon, is presented in Fig. 11. HALO took off from the point marked by the cyan star and flew in the left-front direction, during which it experienced three collisions and was briefly hooked by one of the fans. Despite these collisions, HALO was able to maintain its position and attitude, thereby demonstrating its exceptional maneuverability and robustness. Ultimately, HALO returned to the take-off point and landed safely. Our experiment highlighted the ability of the duct structure to safeguard the UAV in the event of collisions with obstacles, thereby improving the HALO's robust safety features.

V. Conclusion

In this paper, we present a novel design for a safe, servoless, and coaxial UAV equipped with a dual duct structure that enhances both safety and flight efficiency. By incorporating a swashplateless mechanism, the UAV's full attitude can be controlled without the need for traditional actuation methods which is typically based on servo-driven vanes or swashplate. We validate the effectiveness of this approach by demonstrating the UAV's full 3D spatial movement capabilities using a figure-of-eight trajectory, as well as its exceptional disturbance rejection performance when hovering under wind gusts and stick poking. We compare the standard design of HALO with its two variants and show that the duct structure reduces power consumption by 5.23% under the same weight conditions, meanwhile yielding the highest efficiency among the three configurations. Finally, we confirm the safety characteristic of HALO by conducting an actual flight test involving collisions with obstacles.

Authorized licensed use limited to: The University of Hong Kong Libraries. Downloaded on March 28,2024 at 05:31:34 UTC from IEEE Xplore. Restrictions apply.

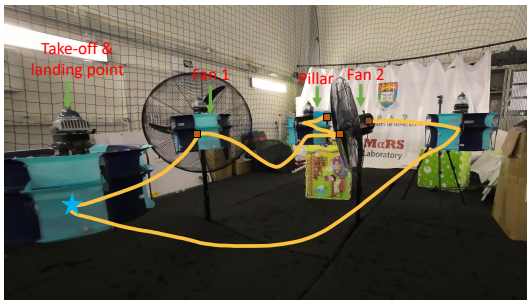

Fig. 10. Virtual flight trajectory in the environment with obstacles and overlaid snapshots of HALO.

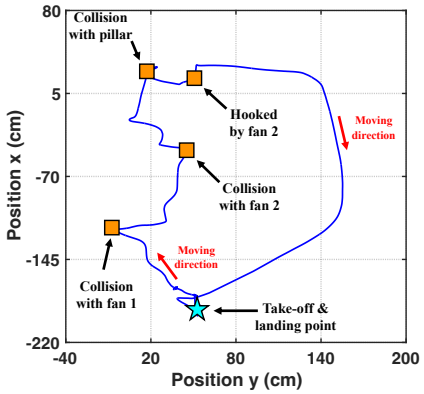

Fig. 11. The actual flight trajectory.

In summary, our proposed design promotes flight safety, power efficiency, and mechanical simplicity, while retaining a similar level of maneuverability and robustness.

ACKNOWLEDGMENT

This work is supported by the General Research Fund of Hong Kong under project 17206920.

REFERENCES

[1] Y. Li, Y. Qin, W. Xu, and F. Zhang, "Modeling, identification, and control of non-minimum phase dynamics of bi-copter uavs," in *2020 IEEE/ASME International Conference on Advanced Intelligent Mechatronics (AIM)*. IEEE, 2020, pp. 1249–1255.

[2] W. Xu and F. Zhang, "Learning pugachev's cobra maneuver for tail-sitter uavs using acceleration model," *IEEE Robotics and Automation Letters*, vol. 5, no. 2, pp. 3452–3459, 2020.

[3] E. K. Bandi, Y. Tamura, A. Yoshida, Y. C. Kim, and Q. Yang, "Experimental investigation on aerodynamic characteristics of various triangular-section high-rise buildings," *Journal of Wind Engineering and Industrial Aerodynamics*, vol. 122, pp. 60–68, 2013.

[4] A. Bondyra, S. Gardecki, P. Gasior, and W. Giernacki, "Performance of coaxial propulsion in design of multi-rotor uavs," in *Challenges in Automation, Robotics and Measurement Techniques: Proceedings of AUTOMATION-2016, March 2-4, 2016, Warsaw, Poland*. Springer, 2016, pp. 523–531.

[5] P. Mukherjee and S. Waslander, "Modelling and multivariable control techniques for small coaxial helicopters," in *AIAA guidance, navigation, and control conference*, 2011, p. 6545.

[6] H. Zhao, C. Bil, and B. Yoon, "Ducted fan vtol uav simulation in preliminary design," in *9th AIAA Aviation Technology, Integration, and Operations Conference (ATIO) and Aircraft Noise and Emissions Reduction Symposium (ANERS)*, 2009, p. 7097.

[7] J. Z. Han, B. Y. Jiang, C. W. Zhuang, and X. C. Du, "Experimental investigation on aerodynamic characteristics of propeller in a ducted-fan type vtol uav," in *Applied Mechanics and Materials*, vol. 711. Trans Tech Publ, 2015, pp. 12–15.

[8] Y. Qin, N. Chen, Y. Cai, W. Xu, and F. Zhang, "Gemini ii: Design, modeling, and control of a compact yet efficient servoless bi-copter," *IEEE/ASME Transactions on Mechatronics*, 2022.

[9] W. Fan, C. Xiang, H. Najjaran, X. Wang, and B. Xu, "Mixed adaptive control architecture for a novel coaxial-ducted-fan aircraft under time-varying uncertainties," *Aerospace Science and Technology*, vol. 76, pp. 141–154, 2018.

[10] A. Ko, O. Ohanian, and P. Gelhausen, "Ducted fan uav modeling and simulation in preliminary design," in *AIAA modeling and simulation technologies conference and exhibit*, 2007, p. 6375.

[11] C. Xu and C. Su, "Dynamic observer-based h robust control for a ducted coaxial-rotor uav," *IET Control Theory & Applications*, vol. 16, no. 12, pp. 1165–1181, 2022.

[12] M. Kartidjo, S. Nugroho, and R. Jiniwangun, "Design and testing of coaxial rotor ducted fan vtol uav," *Jurnal Teknik Mesin*, vol. 24, no. 1, p. 87, 2009.

[13] X. Yuan, J. Zhu, Z. Chen, X. Lu, and J. Meng, "Comprehensive kinematic modeling and analysis of a coaxial helicopter's swashplate mechanism," *Proceedings of the Institution of Mechanical Engineers, Part C: Journal of Mechanical Engineering Science*, vol. 229, no. 10, pp. 1839–1860, 2015.

[14] X. Yuan and J. Zhu, "Inverse dynamic modeling and analysis of a coaxial helicopter's swashplate mechanism," *Mechanism and Machine Theory*, vol. 113, pp. 208–230, 2017.

[15] C. Bermes, S. Leutenegger, S. Bouabdallah, D. Schafroth, and R. Siegwart, "New design of the steering mechanism for a mini coaxial helicopter," in *2008 IEEE/RSJ International Conference on Intelligent Robots and Systems*. IEEE, 2008, pp. 1236–1241.

[16] J. Paulos and M. Yim, "An underactuated propeller for attitude control in micro air vehicles," in *2013 IEEE/RSJ International Conference on Intelligent Robots and Systems*. IEEE, 2013, pp. 1374–1379.

[17] P. James and Y. Mark, "Flight performance of a swashplateless micro air vehicle," in *2015 IEEE International Conference on Robotics and Automation (ICRA)*. IEEE, 2015, pp. 5284–5289.

[18] Y. Ren, F. Zhu, W. Liu, Z. Wang, Y. Lin, F. Gao, and F. Zhang, "Bubble planner: Planning high-speed smooth quadrotor trajectories using receding corridors," in *2022 IEEE/RSJ International Conference on Intelligent Robots and Systems (IROS)*. IEEE, 2022, pp. 6332–6339.

[19] F. Kong, W. Xu, Y. Cai, and F. Zhang, "Avoiding dynamic small obstacles with onboard sensing and computation on aerial robots," *IEEE Robotics and Automation Letters*, vol. 6, no. 4, pp. 7869–7876, 2021.

[20] C. Zheng, Q. Zhu, W. Xu, X. Liu, Q. Guo, and F. Zhang, "Fast-livo: Fast and tightly-coupled sparse-direct lidar-inertial-visual odometry," in *2022 IEEE/RSJ International Conference on Intelligent Robots and Systems (IROS)*. IEEE, 2022, pp. 4003–4009.

[21] W. Xu, Y. Cai, D. He, J. Lin, and F. Zhang, "Fast-lio2: Fast direct lidar-inertial odometry," *IEEE Transactions on Robotics*, vol. 38, no. 4, pp. 2053–2073, 2022.

[22] J.-M. Pflimlin, P. Binetti, P. Soueres, T. Hamel, and D. Trouchet, "Modeling and attitude control analysis of a ducted-fan micro aerial vehicle," *Control Engineering Practice*, vol. 18, no. 3, pp. 209–218, 2010.

[23] T. Ai, B. Xu, C. Xiang, W. Fan, and Y. Zhang, "Modeling of a novel coaxial ducted fan aerial robot combined with corner environment by using artificial neural network," *Sensors*, vol. 20, no. 20, p. 5805, 2020.

[24] H. Malapur, Y. Singh, M. Shendkar, A. Barve, and M. Bedekar, "Diffused casing of drone propeller for reduced operational noise and optimized energy consumption," *Materials Today: Proceedings*, vol. 63, pp. 136–140, 2022.

[25] B. L. Omkar, A. S. A. Doss, and T. C. Michael, "Design and analysis of coaxial ducted propulsion systems of unmanned aerial vehicles," in *IOP Conference Series: Materials Science and Engineering*, vol. 1012, no. 1. IOP Publishing, 2021, p. 012024.

[26] Paulos, James and Yim, Mark, "Cyclic blade pitch control without a swashplate for small helicopters," *Journal of Guidance, Control, and Dynamics*, vol. 41, no. 3, pp. 689–700, 2018.

[27] N. Chen, F. Kong, W. Xu, Y. Cai, H. Li, D. He, Y. Qin, and F. Zhang, "A self-rotating, single-actuated uav with extended sensor field of view for autonomous navigation," *Science Robotics*, vol. 8, no. 76, p. eade4538, 2023. [Online]. Available: https://www.science.org/doi/abs/10.1126/scirobotics.ade4538

[28] Y. Qin, W. Xu, A. Lee, and F. Zhang, "Gemini: A compact yet efficient bi-copter uav for indoor applications," *IEEE Robotics and Automation Letters*, vol. 5, no. 2, pp. 3213–3220, 2020.

[29] S. Gudmundsson, *General Aviation Aircraft Design: Applied Methods and Procedures Ed. 2*. Elsevier Science, 2021.

Authorized licensed use limited to: The University of Hong Kong Libraries. Downloaded on March 28,2024 at 05:31:34 UTC from IEEE Xplore. Restrictions apply.